ARTICLES
https://doi.org/10.1038/s41928-021-00538-4
nature electronics

Check for updates

Strain-resilient electrical functionality in thin-film metal electrodes using two-dimensional interlayers

Chullhee Cho[1,4], Pilgyu Kang[1,2,4], Amir Taqieddin[1], Yuhang Jing[1], Keong Yong[1], Jin Myung Kim[3], Md Farhadul Haque[1], Narayana R. Aluru[1] and SungWoo Nam[1,3] ✉

Flexible electrodes that allow electrical conductance to be maintained during mechanical deformation are required for the development of wearable electronics. However, flexible electrodes based on metal thin films on elastomeric substrates can suffer from complete and unexpected electrical disconnection after the onset of mechanical fracture across the metal. Here we show that the strain-resilient electrical performance of thin-film metal electrodes under multimodal deformation can be enhanced by using a two-dimensional interlayer. Insertion of atomically thin interlayers—graphene, molybdenum disulfide or hexagonal boron nitride—induces continuous in-plane crack deflection in thin-film metal electrodes. This leads to unique electrical characteristics (termed electrical ductility) in which electrical resistance gradually increases with strain, creating extended regions of stable resistance. Our two-dimensional interlayer electrodes can maintain a low electrical resistance beyond a strain at which conventional metal electrodes would completely disconnect. We use the approach to create a flexible electroluminescent light-emitting device with an augmented strain-resilient electrical functionality and an early damage diagnosis capability.

Flexible electrodes are central to the development of flexible electronic devices, including implantable medical sensors, deformable displays and wearable devices for monitoring cognitive or physical performance[1–6]. However, the implementation of practical flexible electronics has been hampered by a lack of robust flexible electrodes that can ensure reliable electrical conduction between the active electrical components under various deformations[7]. Ideally, flexible electrical conductors should offer both electrical conductivity and mechanical flexibility. At present, electrodes based on thin metal films deposited on compliant substrates are commonly used because of their intrinsically high conductivity ($>10^6\,S\,m^{-1}$), ease of integration using conventional manufacturing processes, cost-effectiveness and scalability[8,9]. Thin gold films on polydimethylsiloxane (PDMS), for example, enable flexible electronics applications such as sensitive electronic skins[10], flexible interconnectors between active components on rigid islands[11], biocompatible microelectrodes for neural interfaces[12,13] and soft robotics[14]. However, most electrodes based on thin metal films fracture at small strains (<2%) with low cycles of fatigue failure[15,16]. Metal electrodes on flexible substrates often suffer from rapid surface crack development and eventual interface fracture failure by debonding from the substrate. These sudden and unexpected mechanical fractures lead to electrical failure[17], severely reducing the functional lifespan of flexible devices under various deformations.

After the onset of fracture in metal films, two modes of crack extension are possible: out-of-plane cracking, where cracks extend vertically towards the interface, and in-plane cracking, where cracks occur transversely across the film[18]. Existing approaches to increasing electrode resilience focus on perturbing out-of-plane cracking[19–22], and the contribution of in-plane cracking has rarely been investigated. In-plane crack extension is the primary cause of catastrophic electrical failure due to complete disconnection across the entire film, which results in termination of electrical conductivity[15]. Thus, the ability to modify in-plane crack growth in large-area flexible metal electrodes offers a potential route to augment strain-resilient electrical functionality and the lifespan of flexible metal-based devices.

In this Article, we show that insertion of an atomically thin interlayer of graphene, molybdenum disulfide (MoS_2) or hexagonal boron nitride (hBN) between a thin metal film and a flexible elastomeric substrate can modulate in-plane fracture modes and effectively resist crack extension, substantially improving the electrical robustness of gold and copper metal electrodes against mechanical deformation (Fig. 1a). In the presence of a two-dimensional (2D) interlayer, in-plane crack development of the metal thin film under bending is altered, leading to channelling and a large degree of irregular deflected cracks (Fig. 1b, left). With a conventional bare-metal-based electrode, debonding and straight cracks occur (Fig. 1b, right). The metal–2D electrodes exhibit a slow increase in electrical resistance over a larger strain range, in contrast to conventional metal-based systems, in which sudden rapid increases in electrical resistance occur, followed eventually by abrupt electrical disconnection due to straight crack development[15]. This enables an elongation of the electrical conductance of the metal film with strain, which we term electrical ductility (in analogy to mechanical ductility, which describes elongation of deformation with strain), as well as resistance locking characteristics (Fig. 1c). Our metal–2D electrodes can thus maintain orders of magnitude lower electrical resistance under deformation than conventional electrodes. We illustrate the capabilities of these interconnects by using them to create a flexible electroluminescent light-emitting device that exhibits a gradual decrease in luminous power with increasing applied strain.

In-plane mechanical fracture modulation enabled by 2D interlayers

To study the effect of the 2D interlayer on the sustainability of electrical conductance under mechanical fracture in flexible thin-film metal electrodes, we first characterized the fracture surfaces of

[1]Department of Mechanical Science and Engineering, University of Illinois at Urbana-Champaign, Urbana, IL, USA. [2]Department of Mechanical Engineering, George Mason University, Fairfax, VA, USA. [3]Department of Materials Science and Engineering, University of Illinois at Urbana-Champaign, Urbana, IL, USA. [4]These authors contributed equally: Chullhee Cho, Pilgyu Kang. ✉e-mail: swnam@illinois.edu

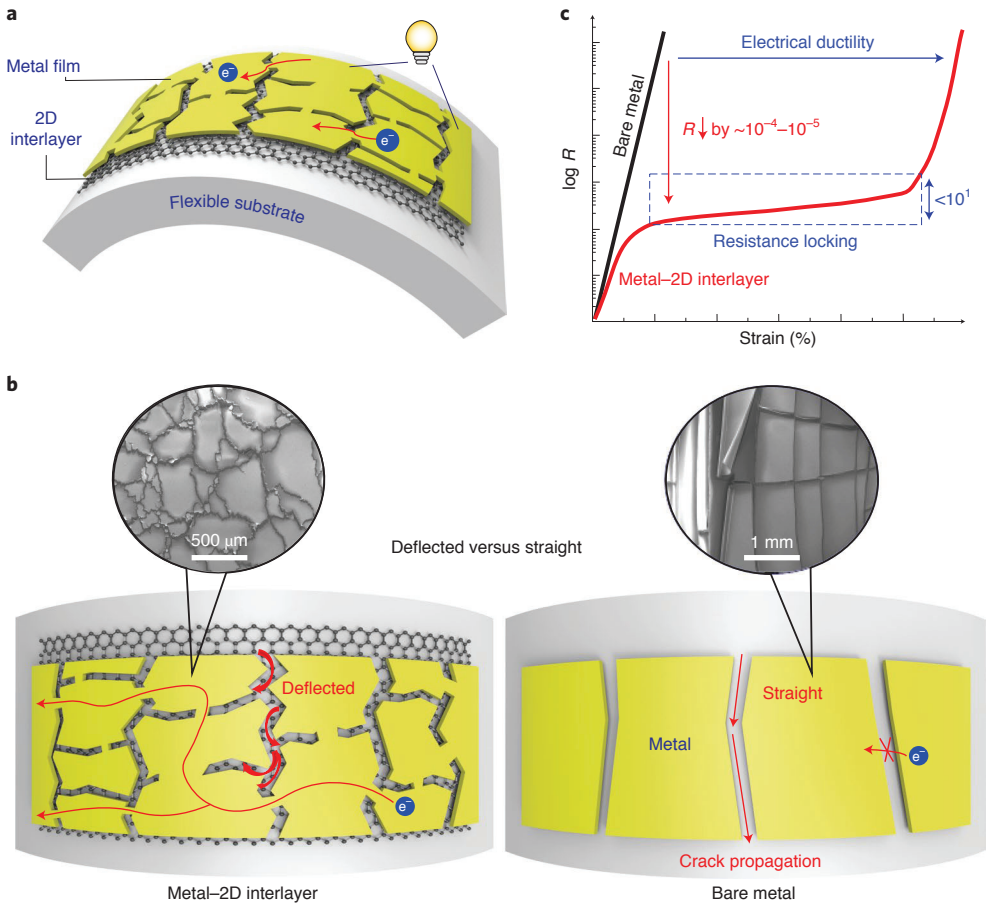

Fig. 1 | Flexible metal electrode achieved by the insertion of a 2D material interlayer. a, Schematic of a flexible metal electrode with an interlayer of atomically thin 2D material. **b**, Schematics of different crack propagation modes on a metal–2D interlayer electrode (left), and on a bare thin metal film electrode (right). Insets: SEM images showing the dominant fracture modes of deflected/multiple cracking (left) and straight/debonding cracking (right). **c**, Conceptual plots of change in resistances (*R*) as a function of applied strain on bare metal electrodes (black) and on metal–2D interlayer electrodes (red).

Au thin films (with an adhesion layer of Ti) on PDMS substrates with and without a graphene interlayer (Methods). Scanning electron microscopy (SEM) images of the fracture surfaces on a conventional thin-film Au/Ti electrode ('bare Au'; Fig. 2a, top) and a single-layer graphene (1LG) integrated Au/Ti electrode ('Au/1LG'; Fig. 2a, bottom) revealed distinct fracture behaviours. On bare Au electrodes, most cracks propagated along straight paths (Supplementary Video 1), eventually resulting in debonding fracture failure (Fig. 2a, top). By contrast, on Au/1LG electrodes, cracks propagated with local zigzag fluctuations (Fig. 2a, bottom and Supplementary Video 2) along the crack growth direction. Crack deflection angles were between 35° and 66° (Supplementary Fig. 1), analogous to the crack kinking angles under mixed-mode loading[23]. Continuous crack deflections led to tortuous crack extension, resulting in the formation of polygonal interconnected domains. To verify the capability to alter fracture modes with a 2D interlayer, we also compared the fracture behaviour of Cu with an adhesion layer of Ti ('bare Cu'), another commonly used metal in flexible electronics, with Cu/1LG and Cu/2LG (2LG, two-layer graphene) areas (Fig. 2b). Straight crack propagation appeared on bare Cu areas, resulting in the film debonding, while multiple cracks with deflected crack edges developed on the Cu/1LG and Cu/2LG areas. These distinct in-plane fracture modes were only apparent in the presence of the underlying graphene interlayer in metal–2D electrodes, regardless of the presence of a Ti adhesion layer (Supplementary Fig. 2). Our results clearly suggest that the underlying 2D interlayer plays a key role in modifying the dominant in-plane fracture behaviour of metal thin films.

Next, we quantitatively analysed crack growth upon bending and investigated the resultant sustainability of the electrical conductance of the metal electrodes. Figure 2c shows changes in crack width as a function of bending strain for both bare Au and Au/1LG electrodes. First, the crack width on the Au/1LG electrode gradually increased with strain, whereas the crack width on the bare Au electrode rapidly accelerated at high bending strains (Fig. 2c). Second, as the strain increased, we observed larger isolated domains on the bare Au compared to the much smaller fracture domains with deflected crack edges on the Au/1LG electrode (Fig. 2d). The average saturated fracture domain size of the Au/1LG electrodes was ~151.6 ± 63.6 μm (Supplementary Fig. 3). Straight cracking behaviour on the bare Au resulted in large isolated domains, while continuous deflected cracking on Au/1LG created much smaller fracture domains. Third, simultaneous monitoring of electrical conductance beyond the bending strain (~7%) at which the bare Au electrode lost its electrical conductance showed that the Au/1LG electrode was still electrically connected (Fig. 2d). We attribute the resultant sustainability of electrical conductance to the presence of progressive cracking and crack bridging induced by the 2D interlayers. Smaller domains with many deflected, narrow cracks resulting from hybrid ductile (zigzag) and brittle (straight)

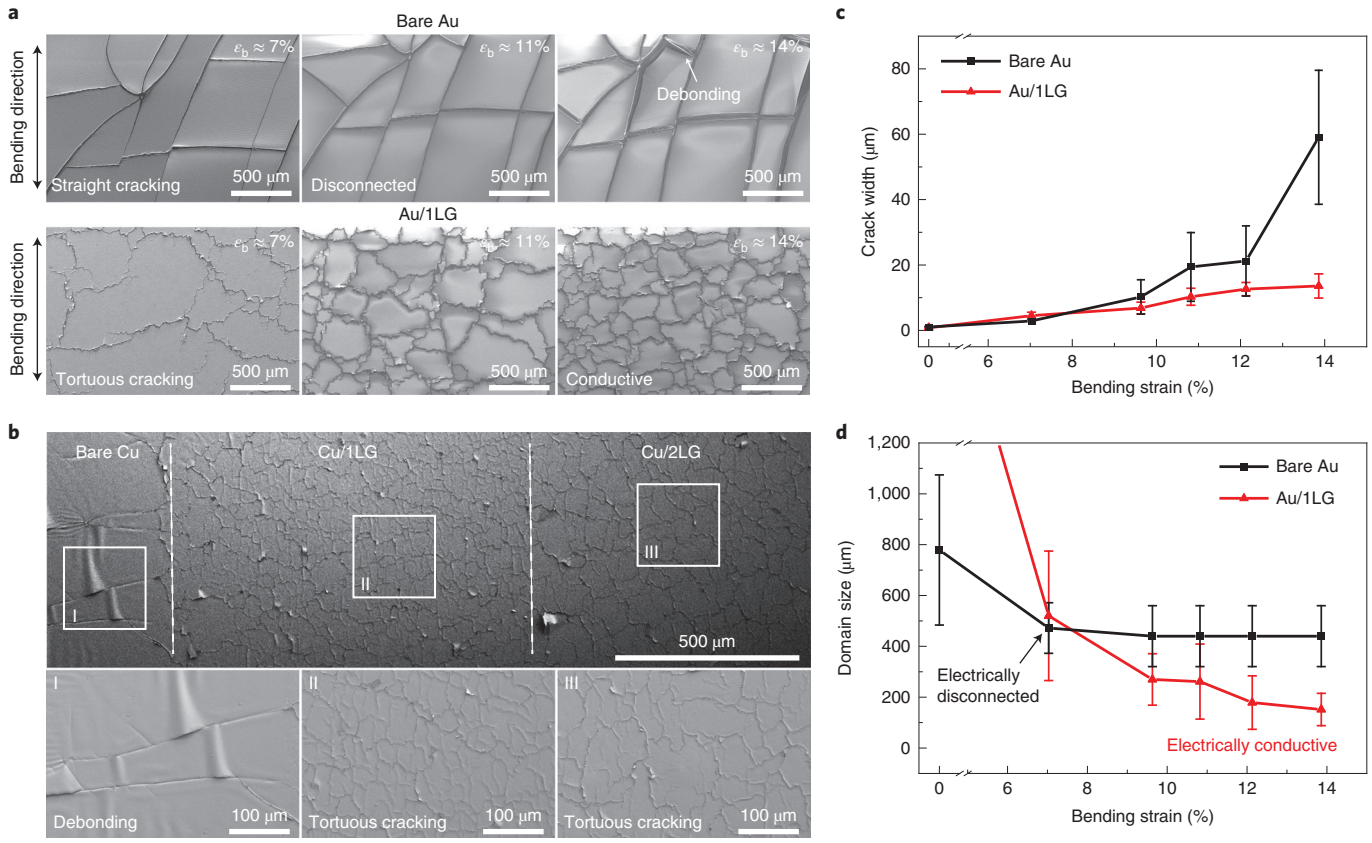

Fig. 2 | Fracture behaviours of thin-film metal electrodes with 2D interlayers. a, Crack progression at various bending strains (ε_b) in a bare Au electrode (top) and a Au/1LG electrode (bottom). White arrow indicates Au film debonding from the PDMS substrate. **b**, Different fracture behaviours observed in bare Cu (I), Cu/1LG (II) and Cu/2LG (III) areas partitioned in one Cu-based electrode. **c**, Crack width on bare Au and Au/1LG electrodes as a function of bending stain. **d**, Fracture domain size on bare Au and Au/1LG electrodes as a function of bending stain. Error bars in **c** and **d** represent one standard deviation.

fracture behaviours on the Au/1LG are more conducive to creating effective conductive paths across the electrode via crack bridging[24] between adjacent domains (Supplementary Fig. 4), which might be more effective with more intrinsically ductile metals. Moreover, early saturation of the domain size on bare Au suggests there was no further strain energy dissipation by cracking, whereas the continuous decrease in the domain size of Au/1LG implies prolonged energy dissipation by progressive cracking. Thus, progressive tortuous cracking behaviour with crack bridging can contribute to maintaining the electrical conductivity beyond a failure strain at which the bare Au electrode showed complete electrical disconnection.

To unveil the underlying mechanism for the unique in-plane fracture behaviour with the 2D interlayers, we carried out detailed characterizations of grain sizes, fracture surfaces and interfaces. First, we characterized the grain sizes of a Au thin film with and without single-layer graphene using high-resolution SEM (Supplementary Fig. 5 and Supplementary Note 'Grain size and metal film quality characterization'). There is no strong or direct correlation between the grain size and fracture domain size—the measured grain sizes of bare Au (68.53 ± 1.2 nm) and Au/1LG (49.16 ± 1 nm) are both at least three orders of magnitude smaller than the average fracture domain size (~151.6 ± 63.6 μm, Fig. 2d) of the Au/1LG electrodes, and the grain size of the graphene (14.78 ± 1.8 μm) is at least an order of magnitude smaller than the average fracture domain. Next, we observed that a heterogeneous buckle network spontaneously formed on the as-prepared Au/1LG electrodes, as confirmed by cross-sectional SEM images and topographic atomic force microscopy scans (Supplementary Fig. 6). We observed a uniform deposited Au film (~202 nm) over graphene on both the flat and buckle-network areas on the as-prepared Au/1LG electrodes (Supplementary Fig. 7). The decrease in interfacial adhesion from the van der Waals interaction of the 2D interlayers, which was confirmed by molecular dynamics (MD) simulations (Supplementary Fig. 8) and an experimental adhesion test (Supplementary Table 1), as well as the increase in film/substrate modulus ratio with the 2D interlayers (Supplementary Fig. 8) promote the formation of a spontaneous buckle network after the metal deposition process (Supplementary Fig. 9 and Supplementary Note 'Modification of mechanical properties of the metal film via the insertion of graphene-interlayers'). We note that our 2D-interlayer engineering approach achieves the desired adhesion regime where we can improve mechanical robustness and prevent the catastrophic fracture failure mode of film debonding from the substrate under strain.

During bending, multiple cracks preferentially initiated at the buckle crests and propagated along the heterogeneous buckle network on the Au/1LG electrodes (Supplementary Fig. 10). Our MD simulation results showed that the cracks occur first on the top metal thin film, and the underlying graphene subsequently fractures at higher strain (Supplementary Fig. 11). The fracture of the underlying graphene along the metal crack paths was characterized by SEM imaging during bending and after removal of the top Au/Ti layer (Supplementary Fig. 12). Intersection and interaction between multiple cracks further delayed complete fracture across the entire metal surface (Supplementary Fig. 10), resulting in macroscopically ductile fractures. By contrast, cracks on bare Au electrodes

propagated straight, perpendicular to the bending direction, without perturbation by the densely packed homogeneous conformal wrinkles prominent on thinner bare Au electrodes (Supplementary Fig. 13), resulting in macroscopically brittle fractures[25] (Supplementary Fig. 14). We observed crack deflection and the resultant tortuous fracture behaviours on Au/2LG electrodes with different thicknesses, with a higher degree of crack deflection and resultant smaller fracture domain sizes on the thicker Au/2LG than on the thinner Au/2LG electrodes (Supplementary Fig. 15), analogous to the length scale effect of film-thickness-dependent fracture behaviours[26,27]. Moreover, our MD simulation results (Supplementary Fig. 9) showed that our in-plane crack deflection mechanism (that is, a buckle-guided fracture mechanism) is caused by the buckle network induced by the 2D interlayer. Our results indicate that discrete buckles can effectively guide crack paths by providing low-energy stress-relief routes due to the localized built-in strain at the crest (buckle-guided fracture) and further perturb in-plane crack development (Supplementary Note 'Crack growth perturbation by buckles versus conformal wrinkles'). Altogether, the 2D interlayer not only enhances intrinsic toughness (Supplementary Fig. 8), which is effective in resisting fracture development by absorbing energy under strain, but also introduces extrinsic toughening mechanisms of crack perturbation/deflection that are effective in reducing the stress and strain experienced at the crack tip. The continuous crack perturbation with crack bridging led by the 2D interlayer is further effective in resisting crack extension to a complete disconnection, enabling the sustainability of electrical conductance of flexible metal electrodes, even in the presence of progressive fractures, rather than the immediate loss of electrical conductance after the onset of surface fracture as in conventional metal electrodes.

Strain-resilient electrical functionality

To further investigate how the unique fracture characteristics imposed by 2D interlayers affect the electrical behaviour, we characterized the electrical resistance as a function of bending strain. The electrical resistance of the metal–2D interlayer electrodes increased gradually upon bending (electrical ductility), in contrast to the abrupt, many orders-of-magnitude increase of resistance observed in bare metal electrodes (Fig. 3a). Moreover, insertion of additional 2D interlayers further reduced the magnitude of resistance change with strain and delayed the complete electrical failure of the electrodes. At ~7% strain (Fig. 3a), at which the resistance of bare Au electrodes increased by more than five orders of magnitude (~100 kΩ), the Au/1LG maintained 10^4 times lower electrical resistance (~10 Ω, blue) and the Au/4LG showed 10^5 times lower electrical resistance (a few ohms, green) than the bare Au electrodes. Furthermore, the electrical failure strain of the Au/4LG electrode ($\varepsilon_{\text{electrical failure}} \approx 24\%$, green curve) was about 400% relative to the electrical failure strain of the bare Au electrode ($\varepsilon_{\text{electrical failure}} \approx 6\%$, red curve). The dependence of electrical failure strains on the number of 2D interlayers is summarized in Fig. 3b. This dependence of electrical failure strain on the number of 2D interlayers is also apparent for Cu-based electrodes (Supplementary Fig. 16). The transformation from abrupt to gradual increase in resistance due to 2D interlayers is analogous to the brittle-to-ductile transition of mechanical properties with temperature. In particular, the extended plateau region with the added 2D interlayer showcases the enhanced 'plasticity' of the resistance, allowing resistance locking with extended regions of stable resistance. This unique strain-resilient electrical functionality is attributed to the 2D-interlayer-induced fracture behaviour of continuous crack deflection and crack bridging, which maintain conductivity at high strain.

To capture the mechanism behind strain-resilient electrical functionality (electrical ductility), we applied the strain-dependent electrical resistance analytical model, which is a function of fracture state with the assumption of the existence of effective conductive paths across cracks[28]. The model relates the progressive increase in the number of cracks to the normalized electrical resistance change

$$\frac{(R-R_0)}{R_0} = \frac{1}{C(k)} \times \frac{\lambda_0}{R_0} \ln\left\{\frac{(N-1)!}{(N-k)^k (N-k-1)!}\right\} \quad (1)$$

where R_0 is the electrical resistance of the crack-free surface, R is the electrical resistance with cracks (k is the number of cracks) in the material at a given strain, N is the saturated number of cracks, λ_0 is a scaling factor that relates the crack opening to the applied strain, and $C(k) = f(\rho_c, t, w, A, k)$ is an electrical ductility parameter as a function of ρ_c (resistivity of the crack), t and w (crack thickness and length), A (an adjustable factor relating the crack propagation rate to the Weibull modulus) and k (Supplementary Note 'Analytical model of electrical ductility'). We utilized the model with our experimental inputs to reproduce the experimental electrical ductility behaviour (Fig. 3a and Supplementary Fig. 17). Based on the fit, we observed that the electrical ductility parameter C increases as the number of 2D interlayers increases. The C parameter for Au/4LG increased more than an order of magnitude compared to that of bare Au (Supplementary Fig. 17). The increase in the value of C indicates that the number of cracks that the materials can withstand before failure becomes higher as 2D interlayers are added (Supplementary Note 'Analytical model of electrical ductility'). Our observation of larger fracture domains on the Cu/2LG areas than on the Cu/1LG areas at a given strain (Fig. 2b) along with the strain-dependent domain size characteristics (Fig. 2d) suggest delayed crack saturation and more gradual crack development as the number of 2D interlayers increases, eventually resulting in higher electrical ductility (increase in C). Insertion of additional 2D interlayers increases the intrinsic fracture toughness (Supplementary Fig. 8), resulting in delayed crack extension through the absorbance of more strain energy as the number of 2D interlayers increases and further reducing the magnitude of resistance change with strain compared to bare metals. We also note that there could be other minor contributing factors, including an additional energy dissipation resulting from potential interlayer sliding between 2D interlayers[29] under strain. We observed that de-adhesion preferably occurred at the graphene/graphene interface on the Au/2LG electrode after the experimental adhesion test (Supplementary Fig. 18); this can reduce the effective strain energy via interfacial sliding when under strain.

To demonstrate the robustness of the metal–2D interlayer electrodes to deformation modes beyond bending, we characterized the electrical behaviour under twisting and fatigue cycling. Consistent with the bending results, during twisting, the metal–2D interlayer electrodes (Fig. 3c) showed enhanced strain-resilient electrical functionality that was dependent on the number of 2D interlayers. The bare Au resistance abruptly increased by three orders of magnitude at a twist angle of 40°. However, the resistance of the Au/1LG electrodes increased by less than one order of magnitude at twist angles up to 90°. Furthermore, the Au/4LG electrodes tolerated twist angles up to 160° with resistance locking remaining in the tens of ohms range, representing an ~400% twist-resilient performance relative to bare Au. We next investigated the robustness of the metal–2D electrodes to fatigue. We measured the electrical resistance of Au/2LG electrodes while subjecting them to 10,000 cycles of bending to half of the electrical failure strain ($\varepsilon_b \approx 11\%$), as shown in Fig. 3d. Our Au/2LG electrode showed reliable electrical performance with its resistance increased by twice its initial resistance and remaining in the approximately tens of ohms range over all cycles.

To explore the generality of our 2D-interlayer approach, we used alternative 2D interlayers including semiconducting MoS_2 and insulating hBN synthesized by chemical vapour deposition

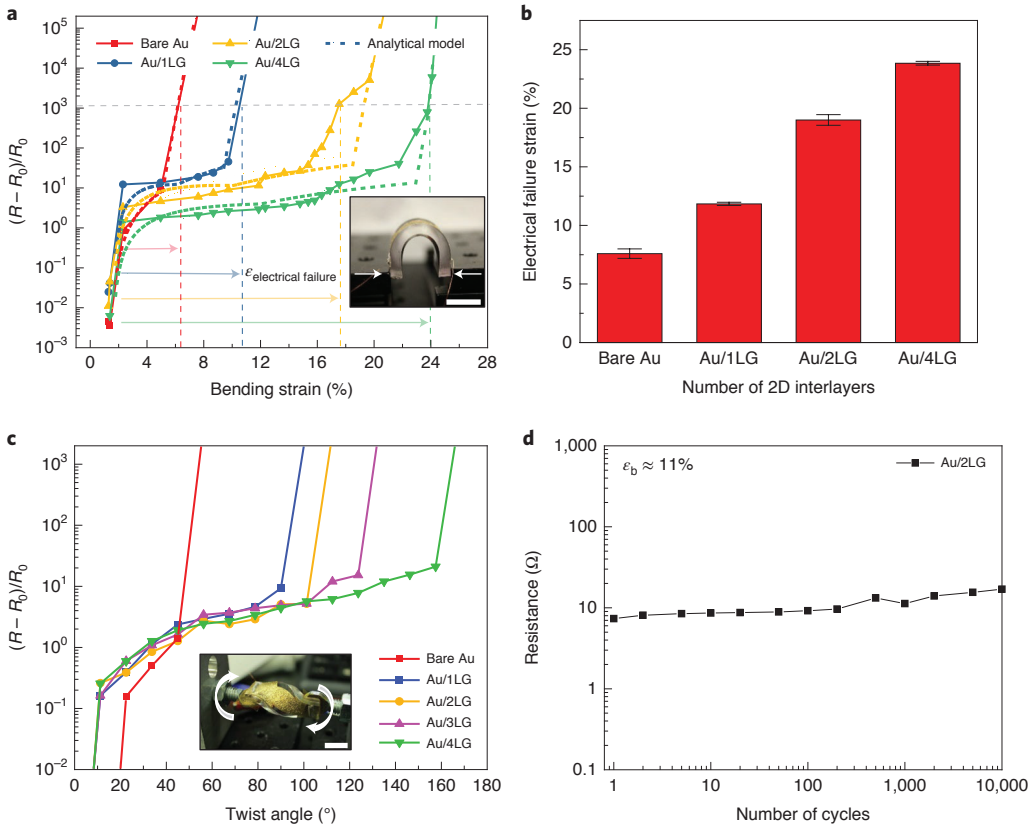

Fig. 3 | Strain-resilient electrical performance with 2D interlayers. a, Electrically ductile behaviours of multilayer-graphene integrated electrodes in response to bending deformation (bending deformation from linear translation displacement shown by the arrows in the image). R_0, initial electrical resistance; R electrical resistance with bending. Scale bar, 10 mm. **b**, Dependence of electrical failure strains under bending on the number of 2D interlayers. Error bars represent one standard deviation. **c**, Electrically ductile behaviour of multilayer-graphene integrated electrodes in response to twist deformation (twist shown by the arrows in the image). Scale bar, 10 mm. **d**, Fatigue test of the Au/2LG electrode under repeated bending strain ($\varepsilon_b \approx 11\%$) up to 10,000 cycles.

(CVD). We observed a similar strain-resilient electrical behaviour under bending (electrically ductility) that depended on the number of 2D interlayers. The electrical failure strain of the Au/4L-MoS_2 electrode was more than 300% that of the bare Au electrodes, and the electrical failure strain of the Au/4L-hBN electrode was more than 240% that of the bare Au electrodes (Supplementary Fig. 16). Our analytical fit (for which the exponential decay model shows good agreement with our experimental observations for various metal–2D electrodes with up to four interlayers) suggests that the electrical failure strain is expected to saturate at above seven interlayers (Supplementary Fig. 19). Moreover, there was no substantial difference in the initial electrical resistance of the as-prepared electrodes with various 2D interlayers (Supplementary Fig. 20), indicating that the underlying 2D materials do not impact the quality of the subsequent deposited metal films. These results indicate that high-strength mechanical properties and the modulated adhesion offered by the 2D materials play a critical role in the strain-resilient electrical performance, which is not primarily due to the electrical conductivity difference arising from the underlying 2D interlayers. The alteration of in-plane fracture provided by the 2D interlayers is the principal mechanism responsible for the strain-resilient electrical characteristic. We attribute the different levels of enhancement of the strain-resilient electrical functionality of Au/MoS_2 and Au/hBN, compared to Au/graphene, to the different mechanical properties of the 2D interlayers, including a reduced effective modulus and toughness[30], as well as electrical conductivity. The overall results suggest that our 2D-interlayer approach can be used with various combinations of metals and 2D atomic layers, including mixed types of 2D materials, which could broaden the general applicability of our 2D-interlayer approach.

Applications to flexible electronics

Finally, we applied our metal–2D interlayer approach to the conducting interconnector in a flexible electroluminescent light-emitting device and measured the strain-dependent luminous power (Supplementary Fig. 21) to demonstrate the utility of metal–2D interlayers in flexible electronics. The electromechanical robustness of our device allowed a high degree of multimodal deformation including bending (Fig. 4a) and twisting (Fig. 4b), without the low-cycle fatigue failure (Supplementary Fig. 22) that occurred with conventional metal-based interconnectors (Supplementary Video 3). Bending-strain-dependent luminous power measurements on the flexible light-emitting device with a conventional metal-based interconnector showed a sudden drop in luminous power at low bending strains (Fig. 4c). In stark contrast, the luminous power of a flexible light-emitting device with a metal–2D interconnector gradually decreased as the applied strain increased. Moreover, the device failure strain at which the flexible light-emitting device became unreadable increased approximately 400% with the metal–2D interconnector (Fig. 4d). Enhancement of device failure strain agrees well with our previous results (Fig. 3) and substantiates the utility of our metal–2D interlayer approach in broad flexible electronics. In addition, the gradual luminous power reduction can be used to diagnose potential device failure. For example, a 40%

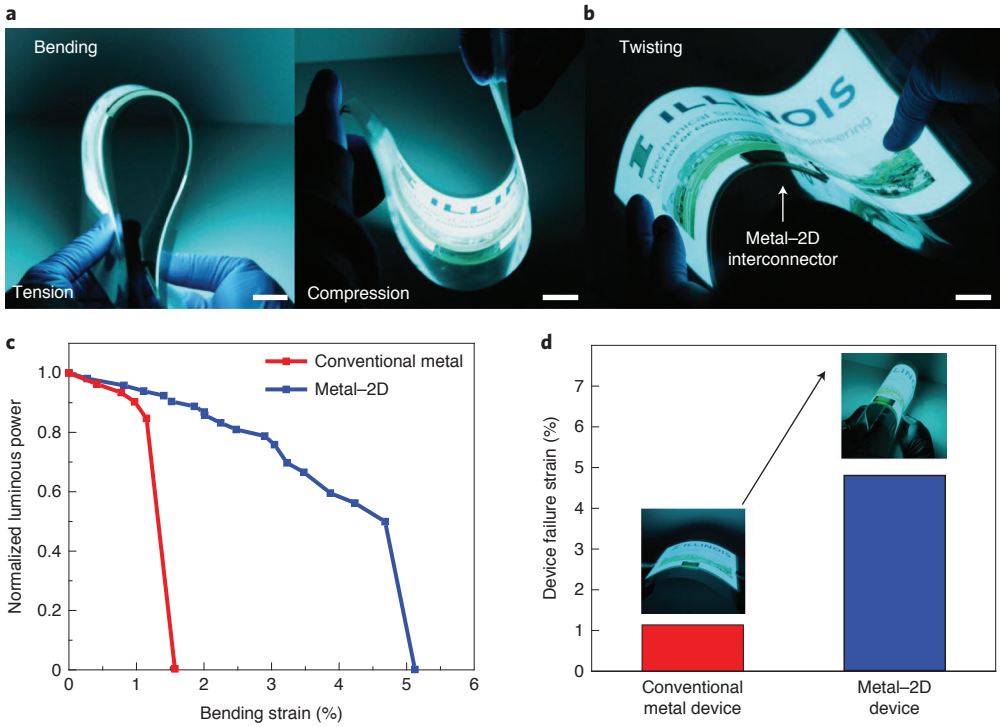

Fig. 4 | Flexible light-emitting device integrated with an electromechanically robust metal–2D interconnector. a, Functionality of a flexible light-emitting device integrated with a Au/2LG-based interconnector under bending deformation modes of tension (left) and compression (right). **b**, Device functionality under a twisting deformation mode. Scale bars, 2 cm. **c**, Normalized luminous power of flexible light-emitting devices integrated with a conventional thin-film metal and a metal–2D interconnector as a function of bending strain. **d**, Device failure strains with a conventional thin-film metal interconnector and the metal–2D interconnector.

decrease in the luminous power of the device (Fig. 4c) can be taken as a pre-alert for partial maintenance or replacement. These early failure diagnosis features arising from the strain-resilient electrical functionality and augmented electrical performance under multimodal deformation could offer advanced electromechanical characteristics to the next generation of wearable and flexible electronics, including bio-implantable electrodes[31] and a human body sensor network[32] where the applications require not only bending, but also folding and twisting modes of deformation.

Conclusion

We have shown that a 2D interlayer can improve the durability of the electromechanical functionality of metal-based flexible electronics. The addition of an atomically thin interlayer between a metal thin film and flexible substrate results in unique strain-resilient electrical characteristics—electrical ductility—through modulation of the in-plane fracture modes of metal thin films from unperturbed straight fractures with brittle behaviour to progressive tortuous fractures with ductile behaviour via a buckle-guided fracture mechanism. The 2D-interlayer electrodes maintain electrical conductivity beyond the failure strain of conventional metal electrodes and further augment the strain-resilient electrical performance with resistance-locking characteristics. To illustrate the capabilities of our 2D-interlayer approach in flexible electronics, we created a flexible electroluminescent light-emitting device integrated with metal–2D interlayers. The device exhibits strain-resilient electrical performance under a high degree of multimodal deformation as well as an early damage diagnosis capability. Our approach is not limited to specific combinations of metals and 2D materials, and could be incorporated into industrial applications that use multilayer laminated structures for flexible and wearable electronics, including conformable and implantable bioelectrodes and foldable/rollable personal electronic devices.

Methods

Sample preparation. Single-layer graphene was synthesized on catalytic 25-μm-thick copper (Cu) foil (Alfa Aesar) using our CVD system (Rocky Mountain Vacuum Tech). CVD-grown single-layer graphene on Cu foil was directly stamped on a flexible elastomeric substrate of 4-mm-thick PDMS and immersed in ferric chloride ($FeCl_3$) etchant solution (CE100, Transene) to etch away the Cu foil. For multilayer graphene interlayers we repeated this laminating transfer method multiple times to artificially stack graphene layers followed by a complete etching of Cu foil and multiple rinsing/cleaning steps with deionized water. The quality of the transferred multilayer graphene was evaluated by two non-destructive optical characterization processes (UV–vis and Raman spectroscopy; Supplementary Fig. 23 and Supplementary Note 'Characterization of multilayer configuration') to ensure there were no substantial defects and chemical residues that might induce undesired fracture behaviours. A 20-nm-thick adhesion layer of Ti and a 200-nm-thick Au layer were then deposited on top of the transferred graphene on a PDMS substrate via electron-beam evaporation. We chose Au, as it is one of the most widely used metals with high electrical conductivity. Samples were also fabricated with CVD-grown hBN on a 25 μm Cu foil purchased from Grolltex following the same sample preparation procedures for Au/hBN samples. CVD-grown MoS_2 on a silicon oxide/silicon wafer was also used to fabricate Au/MoS_2 samples following the same sample preparation procedures, with a modification where MoS_2 layers were transferred onto the PDMS substrates using the water-assisted liftoff transfer method[33].

Characterization of fracture surfaces. To investigate the fracture surfaces of the electrodes, we recorded crack development under bending strain in both bare Au (Supplementary Video 1) and Au/1LG (Supplementary Video 2) electrodes via optical microscopy. The crack deflection angle was measured on the fractured surfaces of the Au/1LG electrodes from images captured from the fracture video. Statistical results (Supplementary Fig. 1) showed that crack deflection occurred between 35° and 66°, with a mean of 52° and a standard deviation of 9.58° extracted by Lorentzian fitting. We also conducted a quasi-static bending test

with an environmental scanning electron microscope (ESEM, FEI Quanta FEG 450 ESEM). The crack development in response to varying bending strain was characterized qualitatively (Fig. 2a,b and Supplementary Figs. 2, 4, 10, 14 and 15) and analysed quantitatively (Fig. 2c,d). Twenty different cracks on both bare Au (Au/Ti) and Au/1LG (Au/Ti/1LG) electrodes were continuously monitored with an increase of bending strain (0–14%) to quantitatively analyse crack width growth (Fig. 2c). Crack width in Fig. 2c is defined as the average distance separating adjacent crack domains. The average domain size (Fig. 2d) was estimated as the root mean square of the diagonal lengths of all the domains[34] presented in ESEM images by using image analysis tools (for example, ImageJ). We note that a few cracks and domains pre-existed on the as-prepared ($\varepsilon_b = 0$) bare Au electrodes due to the residual stress after metal deposition (Fig. 2d). We analysed fracture domain size development with strain on Au/1LG electrodes (Supplementary Fig. 3). Control experiments without a Ti adhesion layer further verified that the 2D interlayer plays a key role of modulating the in-plane fracture modes of metals (Supplementary Fig. 2). A combination of high-resolution field-emission SEM and focused ion beam (FEI Helios 600i) sectioning was used to characterize the cross-section of buckles spontaneously formed on the Au/1LG electrodes (Supplementary Figs. 6 and 7). Atomic force microscopy (Asylum MFP-3D AFM) was used for topography scans (Supplementary Figs. 6 and 13).

MD simulations. We performed MD simulations to theoretically explore the mechanical properties of bare metal and metal–2D interlayers upon bending. Although the MD simulations were limited to nanoscale domains due to the computational complexity, they have shown the ability to produce and explain the mechanical properties of polycrystalline graphene in good agreement with experiment, even when the domain length scale in MD is much smaller than the one in the experiment[35,36]. The simulation model structures of the Au/graphene/PDMS electrodes (Supplementary Fig. 8) are about 13.2 nm long in the x direction and 7.1 nm wide in the y direction. Polycrystalline graphene with different grain sizes was constructed and used for the graphene interlayers inserted between the Au and the PDMS. The initial amorphous PDMS structure with height of 7.2 nm was generated with a density of 0.92 g cm^{-3}. The interaction between C atoms in the graphene is described by an adaptive intermolecular reactive empirical bond order (AIREBO) potential[37]. The interaction between Au atoms is described by a ReaxFF reactive forcefield[38]. The interaction between Mo and S atoms is described by the reactive many-body potential[39]. For the interaction between C and Au atoms, a 6–12 Lennard–Jones potential is used with ε of 0.01273 eV and σ of 2.9943 Å. For the interactions between atoms in the PDMS, the condensed-phase optimized molecular potentials for atomistic simulation studies (COMPASS) potential is employed[40]. The COMPASS potential was optimized from ab initio results and has been used for the investigation of mechanical and thermal properties of PDMS. All MD simulations were performed using the LAMMPS package. The Velocity-Verlet algorithm was used to integrate the equations of motion. A time step of 0.1 fs was chosen. Periodic boundary conditions were applied along the y axis (transverse direction) and free boundary conditions were applied along the other two directions. The Nosé–Hoover thermostat was used to control the temperature. All molecular systems were relaxed with the *NPT* (constant particle number, pressure and temperature) ensemble for 200 ps. Constant pressure (1 atm) and temperature (300 K) were employed during this process. After *NPT* relaxation, the system was relaxed with an *NVE* (constant volume without a thermostat) ensemble for 200 ps. The total energy and temperature of the whole system were monitored during this stage to ensure that the system reached the equilibrium state. At the equilibrium state, a stable structure for the Au/graphene/PDMS electrode was obtained as shown in Supplementary Fig. 8. First, we looked into the adhesion energy of Au/PDMS (interaction energy between Au and PDMS), Au/Ti/PDMS (interaction energy between Ti and PDMS) and Au/Ti/graphene/PDMS (interaction between Au/Ti/graphene and PDMS). The adhesion energy is calculated by[41]

$$W_A = \left(E_{\text{Gold}} + E_{\text{PDMS(+Gr)}} - E_{\text{Gold+PDMS(+Gr)}}\right)/A \quad (2)$$

where E_{Gold} is the total energy of the isolated gold, $E_{\text{PDMS(+Gr)}}$ is the total energy of the isolated PDMS with or without graphene, $E_{\text{Gold+PDMS(+Gr)}}$ is the total energy of the relaxed Gold–PDMS with or without graphene, and A is the area of the interface. All the energies are calculated by averaging the total energy over 50,000 steps after the steady state is reached. The overall adhesion energy results are plotted in Supplementary Fig. 8. Next, the bending test on the electrode was performed under a deformation-control method that is widely used to investigate the bending deformation of 1D and 2D materials[42]. The strain increment is applied to the structure every 10,000 steps. Stress–strain curves obtained from this simulation and toughness, which is the area under the stress–strain curve, are plotted in Supplementary Fig. 8.

Electrical characterization. To investigate the electrical behaviour of bare metal and metal–2D electrodes, we measured electrical resistance as a function of bending strain (Fig. 3a). Bending strain was applied to electrodes using our homemade linear translation stage (shown in the inset of Fig. 3a) with a change of translation distance[43]. An increase in translation distance led to a decrease in the radius of curvature. The radius of curvature (r) was determined by image analysis (ImageJ) and the resultant bending strain was determined based on the analytical formula of $\varepsilon_b \approx t/2r$ (ref. [44]), where t is the total thickness. We defined an electrical failure strain ($\varepsilon_{\text{electrical failure}}$) as the strain at which resistance increased by three orders of magnitude ($>10^3\,\Omega$) relative to the unstrained resistance value (that is, an initial resistance $R_0 \approx 4\,\Omega$ for all electrodes). The three orders of magnitude increase was chosen because this is when the resistance of graphene, which is initially in the range of a few kilo-ohms, might primarily contribute to the overall resistance, indicating the metal layer has failed. We note that when the applied bending strain is less than 2%, the increase in electrical resistance is negligible, ranging between 0.01 and 0.04 Ω. The change in electrical resistance is normalized by R_0 (the value when there is no applied bending strain). We analysed electrical failure strain from more than five sets of Au–graphene electrodes (Fig. 3b). The electrical behaviours of electrodes with Cu–graphene interlayers, Au–MoS_2 interlayers and Au–hBN interlayers were also characterized under bending using the same method (Supplementary Fig. 16). Electrical behaviour under twist deformation was characterized by measuring the electrical resistance during twisting with our homemade twisting stage (shown in the inset of Fig. 3c). Finally, we used an automatic linear translation stage (Thorlabs) to investigate mechanical robustness under cyclic mechanical loading. The electrical resistance of the Au/2LG electrode was monitored as a function of the number of bending–relaxation cycles up to 10,000 cycles. Displacement was applied with a maximum velocity of 2.4 mm s^{-1} and an acceleration of 1.5 mm s^{-2}.

Luminous power measurement. The flexible electroluminescent light-emitting layer consisted of a large monolithic sheet of electroluminescent phosphor layer sandwiched by two dielectric layers of flexible polyvinyl chloride (PVC) polymer between the top and bottom electrodes, with a total thickness of 500 µm. The metal–2D interconnector layer was conformally assembled on top of the flexible light-emitting layer (Fig. 4a,b and Supplementary Fig. 21) so that both components deformed together under bending. We note that the main focus of the demonstration was to show the electromechanical robustness of the interconnector rather than the light-emitting layer itself. To demonstrate the electromechanical robustness of our metal–2D interconnector, the interconnector layer was purposely designed to have a thicker substrate (4 mm) to induce a higher strain than the light-emitting layer (0.5 mm) upon bending. We measured the luminous power of electroluminescent, flexible light-emitting devices equipped with a conventional thin-film metal-based interconnector and a metal–2D-interlayer-based interconnector as a function of the bending strain, as illustrated in Supplementary Fig. 21. Normal force was exerted on one end of the mounted flexible light-emitting device to induce bending deformation. A photodiode power sensor (Thorlabs, S120C and PM100USB) was placed on top of the fixed area (on the opposite end of the mounted flexible light-emitting device) to minimize any bending-induced fluctuation of luminous power during measurements. The measured luminous power during bending was normalized by the unstrained luminous power value.

Data availability

The data that support the plots within this paper and other findings of this study are available from the corresponding author upon reasonable request.

Received: 1 June 2020; Accepted: 5 January 2021;
Published online: 1 February 2021

References

1. Gao, W., Ota, H., Kiriya, D., Takei, K. & Javey, A. Flexible electronics toward wearable sensing. *Acc. Chem. Res.* **52**, 523–533 (2019).
2. Akinwande, D., Petrone, N. & Hone, J. Two-dimensional flexible nanoelectronics. *Nat. Commun.* **5**, 5678 (2014).
3. Hong, G. & Lieber, C. M. Novel electrode technologies for neural recordings. *Nat. Rev. Neurosci.* **20**, 330–345 (2019).
4. Ray, T. R. et al. Bio-integrated wearable systems: a comprehensive review. *Chem. Rev.* **119**, 5461–5533 (2019).
5. Pang, C., Lee, C. & Suh, K. Recent advances in flexible sensors for wearable and implantable devices. *J. Appl. Polym. Sci.* **130**, 1429–1441 (2013).
6. Koh, A. et al. A soft, wearable microfluidic device for the capture, storage and colorimetric sensing of sweat. *Sci. Transl. Med.* **8**, 366ra165 (2016).
7. Robinson, A. P., Minev, I., Graz, I. M. & Lacour, S. P. Microstructured silicone substrate for printable and stretchable metallic films. *Langmuir* **27**, 4279–4284 (2011).
8. Nathan, A. et al. Flexible electronics: the next ubiquitous platform. *Proc. IEEE* **100**, 1486–1517 (2012).
9. Graudejus, O., Go, P. & Wagner, S. Controlling the morphology of gold films on poly(dimethysiloxane). *ACS Appl. Mater. Interfaces* **2**, 1927–1933 (2010).
10. Gerratt, A. P., Michaud, H. O. & Lacour, S. P. Elastomeric electronic skin for prosthetic tactile sensation. *Adv. Funct. Mater.* **25**, 2287–2295 (2015).
11. Rogers, J. A., Someya, T. & Huang, Y. Materials and mechanics for stretchable electronics. *Science* **327**, 1603–1607 (2010).

12. Decataldo, F. et al. Stretchable low impedance electrodes for bioelectronic recording from small peripheral nerves. *Sci. Rep.* **9**, 10598 (2019).
13. Song, E. et al. Flexible electronic/optoelectronic microsystems with scalable designs for chronic biointegration. *Proc. Natl Acad. Sci. USA* **116**, 15398–15406 (2019).
14. Lu, N. & Kim, D. Flexible and stretchable electronics paving the way for soft robotics. *Soft Robot.* **1**, 53–62 (2013).
15. Lacour, S. P., Wagner, S., Huang, Z. & Suo, Z. Stretchable gold conductors on elastomeric substrates. *Appl. Phys. Lett.* **82**, 2404–2406 (2003).
16. Lu, N., Wang, X., Suo, Z. & Vlassak, J. Metal films on polymer substrates stretched beyond 50%. *Appl. Phys. Lett.* **91**, 221909 (2007).
17. Baëtens, T., Pallecchi, E., Thomy, V. & Arscott, S. Cracking effects in squashable and stretchable thin metal films on PDMS for flexible microsystems and electronics. *Sci. Rep.* **8**, 9492 (2018).
18. Beuth, J. L. Cracking of thin bonded films in residual tension. *Int. J. Solids Struct.* **29**, 1657–1675 (1992).
19. Wang, J., Cheng, Q. & Tang, Z. Layered nanocomposites inspired by the structure and mechanical properties of nacre. *Chem. Soc. Rev.* **41**, 1111–1129 (2012).
20. Yin, Z., Hannard, F. & Barthelat, F. Impact-resistant nacre-like transparent materials. *Science* **364**, 1260–1263 (2019).
21. Kim, Y. et al. Strengthening effect of single-atomic-layer graphene in metal–graphene nanolayered composites. *Nat. Commun.* **4**, 2114 (2013).
22. Oh, S. H., Ryu, S. & Han, S. M. Role of graphene in reducing fatigue damage in Cu/Gr nanolayered composite. *Nano Lett.* **17**, 4740–4745 (2017).
23. Hutchinson, J. W. & Suo, Z. Mixed mode cracking in layered materials. *Adv. Appl. Mech.* **29**, 63–191 (1991).
24. Kruzic, J. J., Nalla, R. K., Kinney, J. H. & Ritchie, R. O. Crack blunting, crack bridging and resistance-curve fracture mechanics in dentin: effect of hydration. *Biomaterials* **24**, 5209–5221 (2003).
25. Chowdhury, P. & Sehitoglu, H. Mechanisms of fatigue crack growth—a critical digest of theoretical developments. *Fatigue Fract. Eng. Mater. Struct.* **39**, 652–674 (2016).
26. Suh, Y. D. et al. Random nanocrack, assisted metal nanowire-bundled network fabrication for a highly flexible and transparent conductor. *RSC Adv.* **6**, 57434–57440 (2016).
27. Nam, K. H., Park, I. H. & Ko, S. H. Patterning by controlled cracking. *Nature* **485**, 221–224 (2012).
28. Leterrier, Y., Pinyol, A., Rougier, L., Waller, J. H. & Mnson, J. A. E. Electrofragmentation modeling of conductive coatings on polymer substrates. *J. Appl. Phys.* **106**, 113508 (2009).
29. Zhang, S., Ma, T., Erdemir, A. & Li, Q. Tribology of two-dimensional materials: from mechanisms to modulating strategies. *Mater. Today* **26**, 67–86 (2019).
30. Hess, P. Prediction of mechanical properties of 2D solids with related bonding configuration. *RSC Adv.* **7**, 29786–29793 (2017).
31. Polikov, V. S., Tresco, P. A. & Reichert, W. M. Response of brain tissue to chronically implanted neural electrodes. *J. Neurosci. Methods* **148**, 1–18 (2005).
32. Niu, S. et al. A wireless body area sensor network based on stretchable passive tags. *Nat. Electron.* **2**, 361–368 (2019).
33. Jia, H. et al. Single- and few-layer transfer-printed CVD MoS_2 nanomechanical resonators with enhancement by thermal annealing. In *Proc. 2016 IEEE International Frequency Control Symposium* (*IFCS*) 1–3 (IEEE, 2016).
34. Wu, X. et al. Growth of continuous monolayer graphene with millimeter-sized domains using industrially safe conditions. *Sci. Rep.* **6**, 21152 (2016).
35. Cao, C. et al. Nonlinear fracture toughness measurement and crack propagation resistance of functionalized graphene multilayers. *Sci. Adv.* **4**, eaao7202 (2018).
36. Zhang, P. et al. Fracture toughness of graphene. *Nat. Commun.* **5**, 3782 (2014).
37. Stuart, S. J., Tutein, A. B. & Harrison, J. A. A reactive potential for hydrocarbons with intermolecular interactions. *J. Chem. Phys.* **112**, 6472–6486 (2000).
38. Van Duin, A. C. T., Dasgupta, S., Lorant, F. & Goddard, W. A. ReaxFF: a reactive force field for hydrocarbons. *J. Phys. Chem. A* **105**, 9396–9409 (2001).
39. Liang, T., Phillpot, S. R. & Sinnott, S. B. Parametrization of a reactive many-body potential for Mo–S systems. *Phys. Rev. B Condens. Matter Mater. Phys.* **79**, 245110 (2009).
40. Sun, H. COMPASS: an ab initio force-field optimized for condensed-phase applications—overview with details on alkane and benzene compounds. *J. Phys. Chem. B* **102**, 7338–7364 (1998).
41. Fonseca, A. F. et al. Graphene–titanium interfaces from molecular dynamics simulations. *ACS Appl. Mater. Interfaces* **9**, 33288–33297 (2017).
42. Xiong, S. & Cao, G. Bending response of single layer MoS_2. *Nanotechnology* **27**, 105701 (2016).
43. Chen, H., Lu, B.-W., Lin, Y. & Feng, X. Interfacial failure in flexible electronic devices. *IEEE Electron Device Lett.* **35**, 132–134 (2014).
44. Bae, S. et al. Roll-to-roll production of 30-inch graphene films for transparent electrodes. *Nat. Nanotechnol.* **5**, 574–578 (2010).

Acknowledgements

We acknowledge support from NSF (MRSEC DMR-1720633, ECCS-1935775, DMR-1708852 and CMMI-1554019), AFOSR (FA2386-17-1-4071), NASA ECF (NNX16AR56G), ONR YIP (N00014-17-1-2830) and LLNL (B622092). C.C. acknowledges support from a NASA Space Technology Research Fellow grant (80NSSC17K0149). The simulations were performed using the Extreme Science and Engineering Discovery Environment (XSEDE; supported by NSF grant no. OCI1053575), Blue Waters (supported by NSF awards OCI-0725070, ACI-1238993 and the State of Illinois, and, as of December 2019, by the National Geospatial-Intelligence Agency) and Frontera computing project at the Texas Advanced Computing Center (supported by NSF grant no. OAC-1818253). This research was primarily supported by the NSF through the University of Illinois at Urbana-Champaign Materials Research Science and Engineering Center (DMR-1720633). We are grateful for helpful discussions with A. J. Rosakis and J. A. Rogers.

Author contributions

C.C., P.K. and S.N. conceived the idea, designed experiments and contributed to the discussion and analysis of the results. C.C. performed fabrication and characterization, and wrote the manuscript. A.T., Y.J. and N.R.A. contributed to the analytical and computational analysis. K.Y. worked on the growth of 2D materials and assisted with twist and fatigue tests. J.M.K. worked on fracture monitor videos. M.F.H. performed atomic force microscopy characterizations.

Competing interests

The authors declare no competing interests.

Additional information

Supplementary information The online version contains supplementary material available at https://doi.org/10.1038/s41928-021-00538-4.

Correspondence and requests for materials should be addressed to S.N.

Peer review information *Nature Electronics* thanks Seung Hwan Ko and the other, anonymous, reviewer(s) for their contribution to the peer review of this work.

Reprints and permissions information is available at www.nature.com/reprints.

Publisher's note Springer Nature remains neutral with regard to jurisdictional claims in published maps and institutional affiliations.